published in Materials & Design, 2016, vol 93, 379-387

Assessment of mixed mode loading on macroscopic fatigue crack paths in thick section Al-Cu-Li alloy plate

M.R. Joyce[1], M.J. Starink and I. Sinclair

Materials Research Group, Faculty of Engineering and the Environment, University of Southampton, Southampton, UK
[1] currently at Frazer-Nash Consultancy, UK.

Abstract
High strength, wrought 7xxx (Al-Zn-Mg) and Al-Li based alloys show a propensity for fatigue macroscopic crack deflections aligned along grain boundaries. The present work reports a study on a 3rd generation Al-Li based alloy in the form of a thick AA2297 (Al-Cu-Li alloy) plate, where it was found that although the lithium containing material may indeed be more susceptible to mixed mode grain boundary failure (and by implication crack deflection in conventional tests), the AA2297 alloy fatigue behaviour is mechanistically and functionally equivalent to 7xxx alloy behaviour. It is shown that crack paths are controlled by a combination of crack loading mixity (K_{II}/K_I ratio) and maximum strain energy release rates (expressed as $K_{eq.max}$). Increasing K_{II}/K_I ratio is seen to favour sustained grain boundary failure. Crack growth rate behaviour is discussed in terms of extrinsic and intrinsic components of crack growth resistance. It is shown that the present approach can be successfully applied to predict crack deflection / crack paths for a range of sample geometries and orientations on a range of high strength orthotropic aluminium alloys, including 3rd generation Al-Li based alloys and well-established 7xxx alloys).

Keywords: aerospace alloy; fatigue; crack path; mixity; grain boundary; failure

1. Introduction

Transport legislation concerning emissions is becoming ever more stringent. For example, the Advisory Council for Aviation Research and Innovation in Europe (ACARE) Flightpath 2050 targets of reduced NOx (90%) and CO2 (75%) are driving new thinking in the design and manufacture of the next generation of aircraft. In addition, reduction of recurring costs (especially fuel and maintenance) is a key industry concern, especially for future large-series airframes. Addressing these considerations requires integrated light primary structures and thus aircraft manufacturers are looking into new high strength, damage tolerant materials. Despite the introduction of polymer-based composites, particularly on new-generation wide-bodied airliners, aluminium remains the material of choice for much of the primary structure, including the wings and fuselage, of many types of

commercial airplanes. Thus new or improved light alloys (e.g. Al-Cu-Li) and new manufacturing techniques (e.g. integral metallic architectures) aimed at substantial weight savings are being considered. Particularly 3rd generation Al-Li alloys are superior over more established comparator 2x24 and 7xxx type alloys in term of fatigue crack growth rate [1]. However, the new high strength light alloys are produced through thermomechanical processing and this generally results in directional (orthotropic) mechanical behaviour [2], which is not fully accounted for in fatigue crack growth and fracture design calculations, particularly in terms of physically-meaningful mixed mode failure analysis. Over-conservative fatigue crack growth assumptions can lead analysts and designers to add weight to integrated components. Hence there is a direct need for reliable data on complex orthotropic behaviour and improved understanding of the underlying mechanisms, contributing to the formulation and verification of improved models.

One of the most complex examples of orthotropic behaviour is the macroscopically anomalous crack paths in high strength Al-Li based [3-8] and Al-Zn-Mg based alloys [9,10] under fatigue loading conditions, see Figure 1 (Al-Cu-Li alloy AA2297-T8) and Figure 2 (AA7050-T651 plate). The lack of a fully verified model for this behaviour hampers efficient design with these materials [11], leading to overly conservative designs, or avoidance of materials exhibiting the strongest orthotropic behaviour.

Fatigue testing has revealed macroscopic deflections from nominal mode I paths under both cyclic and monotonic loading: this has been seen for both in-plane testing (L-T and T-L type specimen orientations[*]) [6], and through-thickness testing (L-S and T-S type specimen orientations) in wrought plate materials [7,11]. The former phenomenon has been linked to the propensity for crystallographic fatigue crack propagation in strongly textured alloys containing a high volume fraction of the shearable precipitates, whilst the latter has been linked to grain boundary failure. The incidence of grain boundary failure in age-hardened alloys has been widely discussed in the literature [4,12-33] where the phenomenon has been related to one or more of the following microstructural or micromechanical influences:

1. The presence of equilibrium ageing precipitates, intermetallics or dispersoid phases along grain boundaries, providing favourable sites for void nucleation [13,20,34]. The amount of such precipitates increases with alloying content, as such it increases with alloy yield strength [35].
2. The presence of soft grain boundary precipitate free zones (PFZs) [14,36,37] which may accelerate cracking via strain localisation and stress concentration in the PFZ, the grain boundaries and triple points [12,14].

[*] We use the common notation for directions in a rolled plate: L=longitudinal, T= transverse, S=short-transverse. See also Fig. 4.

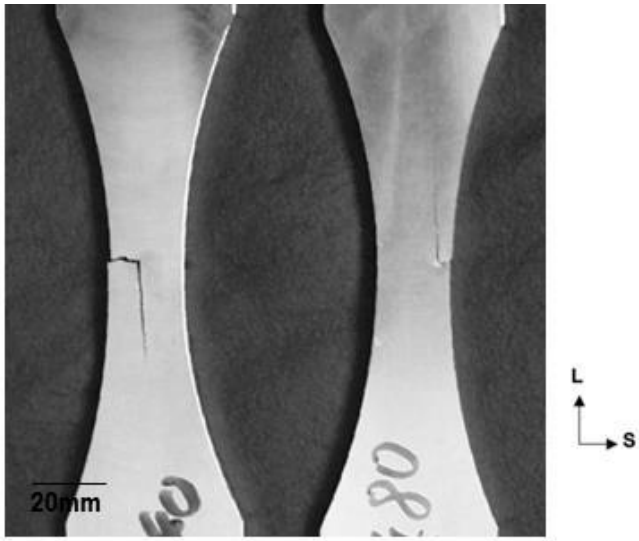

Figure 1: Macroscopic crack deflections in thick AA2297 plate for L-S orientation smooth specimen fatigue tests.

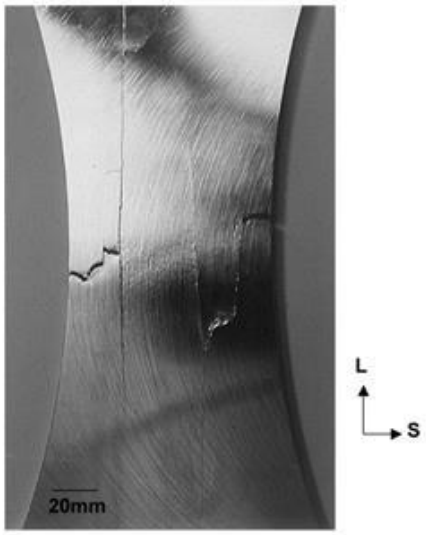

Figure 2: Macroscopic crack deflection in thick AA7050 plate for L-S orientation smooth specimen fatigue tests.

3. Matrix precipitate shearability and the associated tendency for inhomogeneous planar deformation, which may then promote grain boundary failure via stress/strain concentration at slip band - grain boundary intersections [6]. This effect is minimised in third generation Al-Li based alloys by virtue of the reduced (in comparison to 1st and 2nd generation Al-Li based alloys) Li content which tends to avoid the formation of the highly shearable δ′ Al_3Li precipitates.
4. Environmental interactions, such as hydrogen embrittlement of the grain boundary and stress corrosion cracking processes: for the 2090 Al-Cu-Li alloy the effect of H content was shown to be very small however [38].
5. Impurity element segregation to the grain boundary (e.g. due to Pb and Bi), with the potential influences of alkali metal segregation in Al-Li alloys (particularly Na, K, C) being noted [30].
6. Lithium segregation at grain boundaries [16].
7. The orientation relationship between a growing crack in one grain and the possible slip planes a grain ahead of it (i.e. local texture), which can either favour progression into the new grain or deflection along a grain boundary [21,39].

Whilst a distinct body of information is available on grain boundary failure in aluminium-based alloys, there are a number of conflicting reports concerning the controlling interactions in different situations. In particular, the role of grain boundary PFZ strain concentration during fracture or fatigue crack growth is unclear. PFZ strain concentration with amplifications up to a factor of 10 occur during plastic flow in Al-based materials [34]. The

significance of the shear loading of boundary PFZs may be identified from the marked decrease in tensile ductility that may occur when tensile testing wrought material at ~45˚ to the predominant grain boundary plane [40], i.e. the optimum orientation for shear deformation within soft boundary layers constrained between age hardened grain interiors. Sensitivity to shear loading may then be seen as critical to the development of deflected crack paths in conventional test specimens, as propagation must then occur under mixed mode crack tip conditions.

The underlying propensity for PFZ strain concentration to occur for a given material/heat treatment combination is related to the strength differential between the bulk grain and grain boundary material [12,14], i.e. $\Delta\sigma = \sigma_{grain} - \sigma_{PFZ}$, where σ_{grain} is the flow strength of the precipitate hardened grain interiors, and σ_{PFZ} is the PFZ flow strength, which may retain significant solute strengthening. For most high strength 7xxx-series alloys, a reasonable estimate for σ_{PFZ} is of the order of 100 to 200 MPa [31,41], suggesting $\Delta\sigma$ values of the order of 300 MPa for heat treatable Al-alloys of comparable strength levels.

The main classes of high strength Al based alloys used in aerospace applications are 7xxx (Al-Zn-Mg based) alloys and 3rd generation Al-Li based alloys [2,42]. For the work in this report, the 3rd generation Al-Li based AA2297 alloy was selected and additional data from a previous study on the AA7050 alloy are included in the analysis. The AA2297 alloy is a typical example of a 3rd generation Al-Li based alloy incorporating both Mn and Zr dispersoid forming elements (see Table 1), which has been shown to be beneficial for the toughness and particularly the fracture toughness in the short-transverse direction, which is very often a critical direction for certain applications such as very thick plates applications [43,44]. TEM work on AA2X97 alloy [45,46] and various related alloys [2,47] have shown that T1 precipitates are the main strengthening phase. Global fatigue crack growth rates of AA2X97 and other 3rd generation Al-Li alloys are extensively reviewed in [1].

In the present work we consider fatigue crack paths in the AA2297 alloy and compare them with earlier work [9] on an AA7050 alloy, particularly the effects of shear loading on grain boundary failure and the propensity for sustained co-planar mixed mode crack growth along grain boundaries that must occur during macroscopic crack deflection in conventional (mode I loaded) L-S samples studied. The aim of this work is to provide a coherent and generally applicable methodology of characterising the anomalous macroscopic crack path behaviour in these orthotropic high strength light alloys with weak grain boundaries, and provide the data and mechanistic insights for predictive models. The present work does not include nanoscale characterisation (e.g. through transmission electron microscopy) of grain boundaries, and for general assessments of grain boundaries in related 3rd generation Cu and Zr containing Al-Li alloys the reader is referred to [37,48,49,50].

2. Experimental

2.1 Materials

Thick AA2297-T8 plate (104 mm gauge) samples were provided by Centre de Recherche à Voreppe (CRV), France. Nominal chemical compositions and mechanical properties are shown in Tables 1 and 2 respectively; also compositions and properties of AA7050 referred to in Section 4 are included. The AA2297-T8 alloy had been produced through conventional casting, followed by homogenization heat treatment, solution heat treatment, water quenching, stretch and artificial ageing to a T8 condition. Figure 3 shows a typical optical micrograph of the elongated grain structure. Optical micrographs show the material was predominantly unrecrystallised with grain dimensions of about 2000 μm × 2000 μm × 70 μm (L×T×S); and, in the unrecrystallised areas, an equiaxed sub-grain structure with size ~10 μm. Detailed microstructural characterization of these types of artificially aged Al-Cu-Li-Mn-Zr alloys is available in the literature (see e.g. [2,15,44,45,51] and references therein).

	Cu	Li	Mn	Zn	Mg	Zr	Fe*	Si*	Al
AA2297	2.9	1.2	0.3	-	-	0.1	0.05	0.05	Bal.
AA7050	2.3	-	-	6.2	2.3	0.1	0.1	0.1	Bal.

Table 1 Nominal compositions (wt%) of AA2297 & AA7050 (indicates max. values)*

	Direction	$\sigma_{y(0.2)}$ (MPa)	σ_{UTS} (MPa)	el%
AA2297-T8	L	415	450	12.5
	T	415	455	8.5
AA7050-T7651	L	460	514	10
	T	454	524	8

Table 2 Typical mechanical properties for AA2297-T8 plate in 104mm gauge, and AA7050-T7651 plate. $\sigma_{y(0.2)}$ is the 0.2% proof stress, σ_{UTS} is the ultimate tensile stress and el% is the elongation at fracture.

Figure 3: LS plane section of AA2297 plate grain structure (optical micrograph).

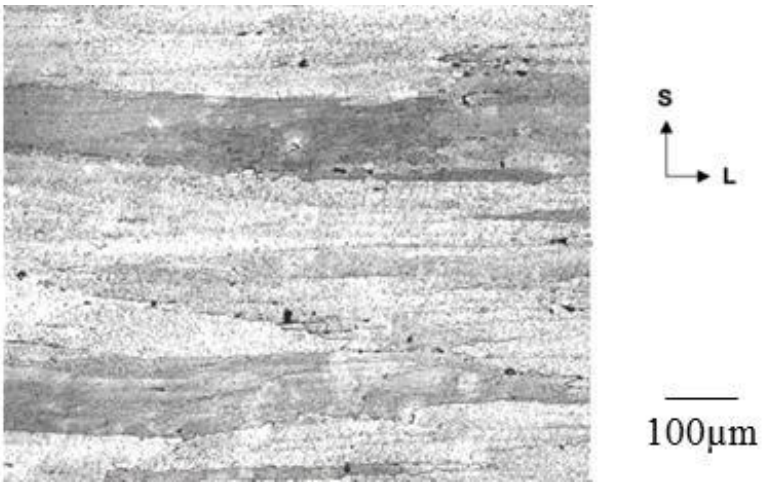

2.2 Experimental Design

In highly orientated microstructures such as the plate considered here, the incidence of intergranular failure under nominal mode I testing may be differentiated into the so called crack blunting (L-S/T-S type), crack delamination (S-L/S-T type) and crack divider (L-T/T-L) configurations, as illustrated in Figure 4. In this study, samples in the S-L orientation were considered, consistent with the crack plane/orientation taken up after crack deflection has occurred in L-S type coupons, as shown in Figures 1 and 2. Mixed mode fatigue testing was carried out in the S-L orientation using 5 mm thick compact shear specimens (CSS) and a special loading fixture (similar to those described in [9,11,52]) that allowed various combinations of normal (mode I) and shear (mode II) crack loading, as shown in Figure 5.

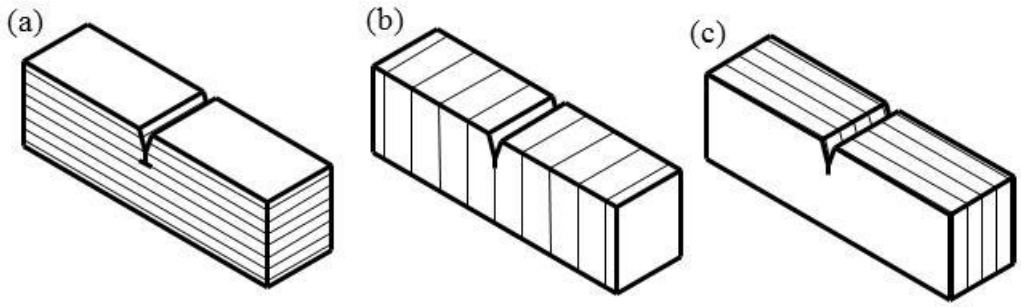

Figure 4: Schematic illustration of crack interaction with weak planar grain boundaries: (a) L-S/T-S orientations, "crack arrest", (b) S-L/S-T orientations, "crack delamination", and (c) L-T/T-L orientations, "crack divider".

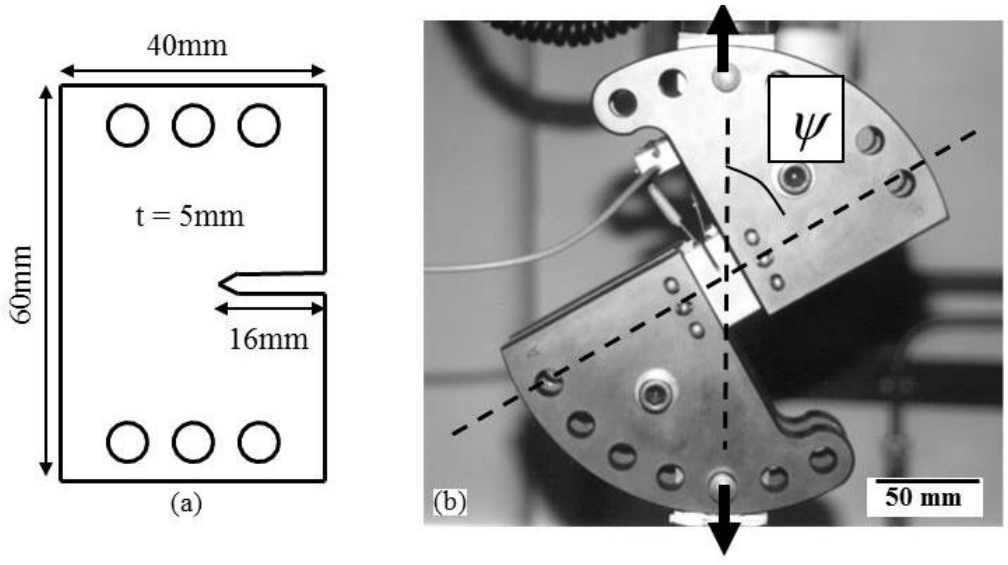

Figure 5: (a) Compact shear sample dimensions, and (b) mixed mode loading rig.

The crack tip stress intensity factors for a straight crack in such samples are given by:

$$K_{I,II} = \frac{P\sqrt{\pi a}}{Wt} F_{I,II} \quad (1)$$

where P is the applied load a is the crack length, W is the overall sample width and t is the sample thickness whilst F_I and F_{II} are appropriate compliance factions for modes I and II, respectively. Analytical expressions for these compliance factions are [52]:

$$F_I = \frac{\cos\psi}{1-\frac{a}{W}}\sqrt{\frac{0.26+2.65\left(\frac{a}{W-a}\right)}{1+0.55\left(\frac{a}{W-a}\right)-0.08\left(\frac{a}{W-a}\right)^2}} \tag{2}$$

$$F_{II} = \frac{\sin\psi}{1-\frac{a}{W}}\sqrt{\frac{-0.23+1.40\left(\frac{a}{W-a}\right)}{1-0.67\left(\frac{a}{W-a}\right)+2.08\left(\frac{a}{W-a}\right)^2}} \tag{3}$$

where ψ is the angle of fixture rotation, as shown in Figure 5. These expressions are valid for $0.5<a/W<0.7$. (The sample geometry employed in this work is slightly modified from that considered in [52], however Finite Element (FE) modelling showed these compliance functions are still valid within ~3%.)

In previous work from our group [9] it was suggested that the incidence of macroscopically sustained grain boundary propagation in AA7050 plate could be characterised in terms of the mode mixity ratio, K_I/K_{II}, and absolute K_I and K_{II} levels. For convenience, the absolute modal stress intensity levels were summed in terms of a strain energy release equivalent co-planar stress intensity factor [27], K_{eq}:

$$K_{eq} = \sqrt{(1-\nu^2)K_I^2 + (1-\nu^2)K_{II}^2 + (1+\nu)K_{III}^2} \tag{4}$$

where v is the Poisson ratio. We define $K_{eq.max}$ as the initial maximum K_{eq} value at the start of crack propagation. Various combinations of mode mixity ratio, R-ratio and initial $K_{eq.max}$ level were considered in the present work. Specifically, mode mixity ratios of 0, 0.35, 0.7 and 1.4, in combination with initial $K_{eq.max}$ values of 5, 7, 10 and 15 MPa$\sqrt{}$m and R-ratios of 0.1 and 0.5 were considered. Tests were performed at a range of specific $K_{eq.max}$ values, as previous work [9] indicated that the incidence of macroscopically sustained mixed mode crack growth along grain boundaries may be strongly determined by this parameter.

Fatigue cracks were initiated from slits introduced using a low speed diamond saw to give an initial notch root radius of ~150μm. In this work fatigue pre-cracking is specifically avoided because it is likely to introduce stresses due to crack face contact when mode II opening components are applied. Such additional stress, which can not be measured, would adversely influence our analysis of the relation between stresses and crack growth direction. Tests were carried out under constant applied load amplitude and hence increasing stress intensity conditions. All fatigue testing was performed at room temperature in laboratory air using an Instron 8502 servo hydraulic machine to apply cyclic loading at a frequency of 20Hz. During testing, crack growth was monitored using the two-point direct current potential drop (d.c.p.d.) technique, thereby allowing determination of crack growth rates.

To enhance reproducibility, we used one plate for all experiments. The entire plate was consumed producing mechanical testing examples. To achieve the maximum possible information for the analysis the maximum number of tests with different $K_{eq,max}$ and K_{II}/K_I were performed, with one sample being reserved for a duplicate test to check reproducibility.

Post-failure analysis was carried out optically to identify macroscopic fatigue crack paths, whilst fracture surfaces were examined using a scanning electron microscope (SEM) operated in secondary electron imaging (SEI) and backscattered electron imaging (BEI) modes. All SEM work was performed using a JSM 6500F field emission gun scanning electron microscope (FESEM) manufactured by Jeol (Japan). The BEI mode was employed to reveal the intermetallic particles which, due to their Cu or Mn content provide a bright contrast.

3. Results

• Macroscopic crack paths

Figure 6 shows the samples post fatigue testing for four K_{II}/K_I ratios; for definition of the orientations of cracks and loading axes, the reader is referred to Eqs. 2-4 and Fig 5b. As expected, those tests carried out under pure mode I loading produced macroscopically straight crack co-planar cracks. Fracture paths produced under mixed mode loading are illustrated in Figure 6 for the various K_{II}/K_I =1.4 tests in order of ascending initial $K_{eq.max}$. Macroscopic crack deflection was observed in tests carried out at low initial $K_{eq.max}$ levels ($\leq$ 7 MPa$\sqrt{m}$), consistent with conventional understanding of crack path development under mixed mode loading. However, in tests performed at higher initial $K_{eq,max}$ values, cracks grew in a macroscopically straight manner, with propagation remaining co-planar with the starter slit and the plane of grain boundary alignment within the material.

The controlling influence of initial $K_{eq,max}$ on crack path for a given mixity level is evident in Figure 6: co-planar crack growth is observed for tests at R = 0.1 and 0.5 at the same initial $K_{eq.max}$ of 10 MPa$\sqrt{m}$, whilst similar macroscopic crack deflections occurred at the lower initial $K_{eq.max}$ level of 7 MPa$\sqrt{m}$. Measurement of the initial macroscopic deflection angle, θ, (averaged over the first 1 mm of crack growth[*]) in Figure 6 shows that for K_{II}/K_I =1.4 tests at R=0.1, θ changes from 48° at low $K_{eq.max}$ to 0 a high $K_{eq.max}$ ($K_{eq.max}$ of 10 MPa$\sqrt{m}$ and higher). These measured deflection angles are shown as a function of K_{II}/K_I in Fig. 7.

[*] Ideally, deflection angles should be based on the first, vanishingly small increment of crack extension. Local crack path variability occurring at the scale of the grain structure in the present commercial plate materials however made such precise assessment problematic.

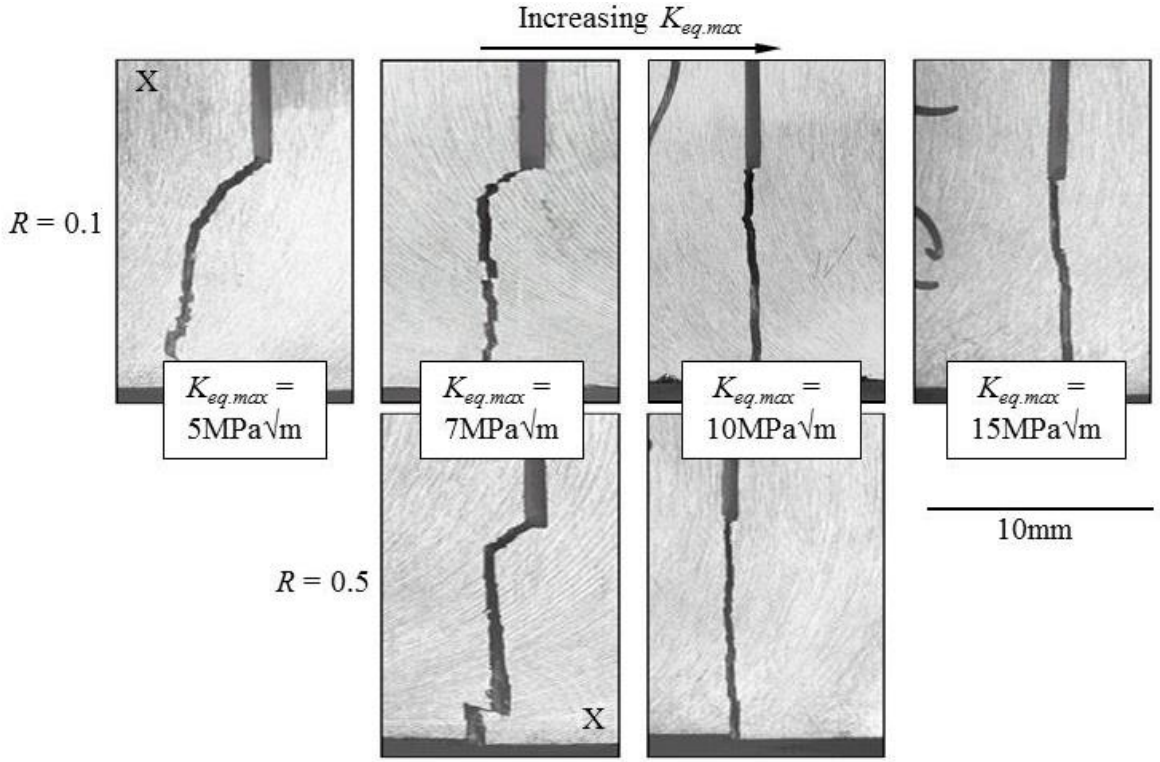

Figure 6: Effect of applied $K_{eq.max}$ and R-ratio on initial crack growth direction in samples tested at K_{II}/K_I =1.4 (samples shown in rows of equal R-ratio and columns of equal $K_{eq.max}$).

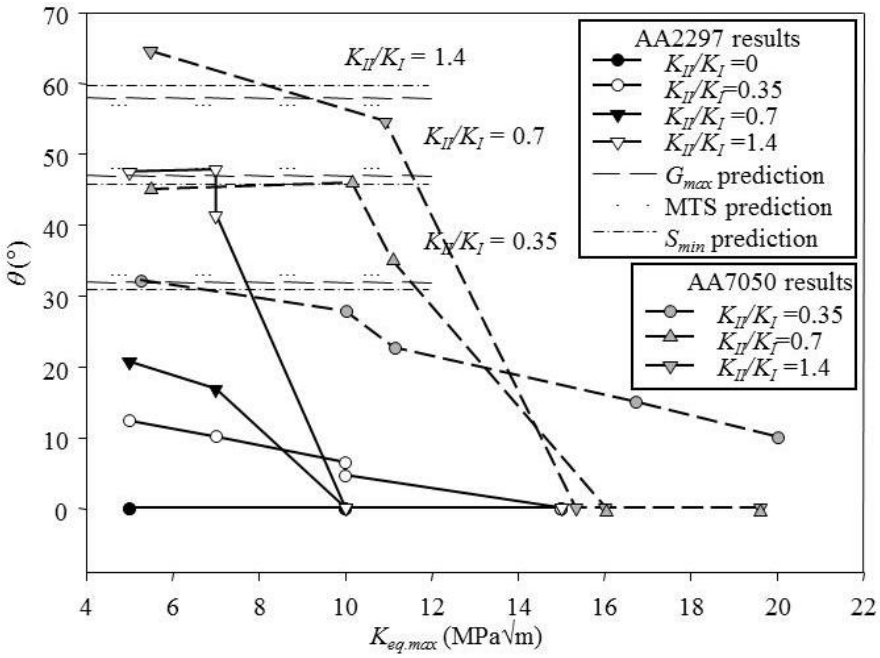

Figure 7: Initial crack propagation angle, θ, as a function of initial K_{eqmax} for AA2297 And AA7050. Also shown are MTS, S_{min} and G_{max} predictions.

Functionally similar crack path behaviour was seen at all tested mixity levels, with substantial crack deflection at low K_{II}/K_I, and θ decreasing with increasing K_{II}/K_I. Measured θ plotted in terms of the initial applied $K_{eq.max}$ for all tests are shown in Figure 7. At low initial $K_{eq.max}$ levels ($\leq$ 7 MPa$\sqrt{m}$), crack deflection is observed under all mixed mode conditions, with the value of θ increasing with increasing mixity level. Particularly, at $K_{eq.max}$ of 5 MPa$\sqrt{m}$, θ increases from 12° at K_{II}/K_I = 0.35 to 21° at K_{II}/K_I = 0.7 to 48° at K_{II}/K_I = 1.4. At higher initial $K_{eq.max}$ levels ($\geq$10 MPa$\sqrt{m}$), the magnitude of crack deflection was significantly reduced in all mixed mode conditions, tending towards co-planar propagation (θ = 0°). In all cases where direct comparison could be made, no difference was noted in crack path morphology between samples tested at load ratios of 0.1 or 0.5 for a given mixity and initial $K_{eq.max}$ level.

Equivalent macroscopic crack path results obtained previously for AA7050 are also shown in Figure 7. Compared to these, the Al-Cu-Li alloy appears more susceptible to sustained co-planar propagation, typically becoming established at $K_{eq.max}$ levels of the order of 5MPa$\sqrt{m}$ lower than in the AA7050 at comparable K_{II}/K_I levels. In addition to the experimentally observed values of θ, predicted crack deflection angles are also shown in Figure 7 for three common failure criteria: (1) maximum tensile stress (MTS) control [53], (2) minimum strain energy density control [54] (S_{min}), and (3) maximum strain energy release rate control (G_{max}). Only in tests performed at low initial $K_{eq.max}$ values do the observed values of θ tend towards the various predictions. At higher $K_{eq.max}$ values the crack propagation angle deviated substantially from these predictions, i.e. the crack growth direction becomes anomalous, with crack progression direction showing an increasing tendency to become aligned with the (weak) grain boundaries as $K_{eq.max}$ increases. Overall it may be seen that whilst crack deflection at low initial $K_{eq.max}$ levels in the 7xxx-series material did approach the theoretical predictions, deflection angles in the AA2297 tests were relatively low, even at the lowest $K_{eq.max}$ levels tested.

Figure 8 shows crack growth rates from tests at both R-ratios under pure mode I and under mixed mode loading conditions where fully co-planar growth was observed (initial $K_{eq.max} \geq$ 10 MPa$\sqrt{m}$ for K_{II}/K_I = 0.7 and 1.4, and for initial $K_{eq.max} \geq$ 15MPa$\sqrt{m}$ for K_{II}/K_I = 0.35). The crack growth rates are expressed in terms of ΔK_{eq} to allow direct comparison of the mixed mode and mode I results, showing faster crack growth in tests performed at the higher R-ratio, particularly evident for the slope change at $K_{eq.max}$ ~5 MPa$\sqrt{m}$. At R = 0.1, a band of crack growth rates (covering a factor of ~4 in da/dN) is observed for the various load mixities, with no simple influence of K_{II}/K_I evident (individual mixed mode growth rate curves are seen to rise and fall in relation to the mode I trend). At R = 0.5, there is more consistent indication of faster crack growth rates under mixed mode loading compared to the mode I baseline at R = 0.5 (by a factor of ~3 typically).

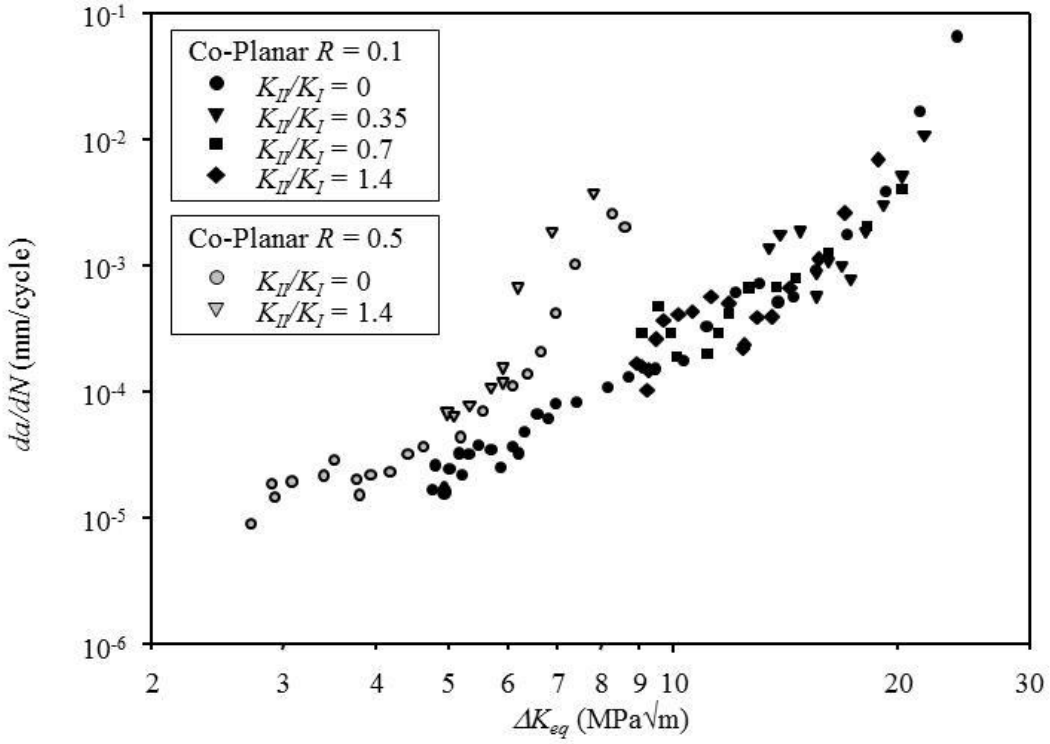

Figure 8: Crack growth rates measured in AA2297 plate.

The crack growth rates in Figure 8 are within the range of crack growth rates observed for other aluminium aerospace alloys of comparable strength [1]. Crack growth rates in our AA2297-T8 plate are very similar to reported crack growth rates in 7050-T7 and 7055-T7 plates, but faster than reported crack growth rates in 2099-T8 and 2055-T8 plates [1].

• *Microscopic crack behaviour*

The fracture surfaces at a range $K_{eq.max}$ levels and R ratios were analysed using SEM. Corresponding secondary electron imaging (SEI) and backscattered electron imaging (BEI) of fracture surfaces produced at $K_{eq.max}$ levels of 5 and 15MPa√m under mode I loading are shown in Figure 9 for an R-ratio of 0.1 (similar behaviour was observed at an R-ratio of 0.5). At low applied stress intensity factors, cracks appear to be transgranular, generally exhibiting crystallographic features, see Figure 9(a). In contrast, fatigue crack propagation at $K_{eq.max}$ = 15MPa√m appears largely intergranular, exhibiting a more rumpled morphology, as shown in Figure 9(b). Comparing the BEI images in Figures 9(c) and 9(d) respectively, significantly more intermetallics are evident on the fracture surface at the higher stress intensity level (revealed as bright particles due to the high content of elements that are substantially heavier than the Al-rich matrix [13,55]).

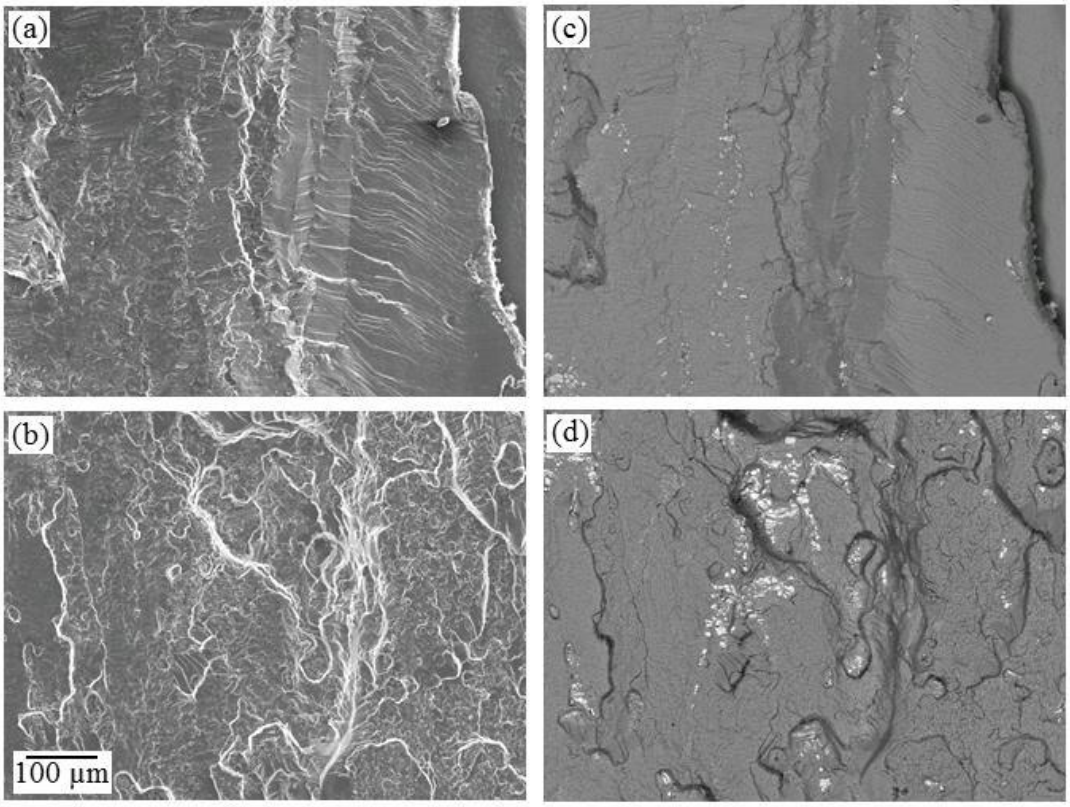

Figure 9: Fracture surfaces under pure mode I loading at $R = 0.1$: (a) SEI, $K_{eq.max} = 5$ MPa√m, (b) SEI, $K_{eq.max} = 15$ MPa√m, (c) BEI, $K_{eq.max} = 5$ MPa√m, (d) BEI, $K_{eq.max} = 15$ MPa√m.

Figure 10 shows a similar set of images of the fracture surfaces produced under mixed loading. The presence of crystallographic features indicated that, as in the pure mode I tests, crack propagation at low $K_{eq.max}$ levels occurred principally by a transgranular mechanism. At high $K_{eq.max}$ levels, the fracture surface exhibited a rumpled morphology indicative of intergranular propagation, similar to that produced under mode I loading, although qualitatively it appeared somewhat flatter. Whilst the mixed mode tests again showed an increasing coverage of grain boundary intermetallics for fracture surfaces at higher $K_{eq.max}$ levels, distinctly fewer intermetallics were evident in the $K_{II}/K_I = 1.4$ tests compared to the mode I loading at equivalent $K_{eq.max}$ levels (illustrated by Figures 9(d) and 10(d) in particular, and confirmed by more extensive and systematic fracture surface imaging).

Figure 11 shows high magnification images of the fracture surfaces during high $K_{eq.max}$ propagation, highlighting regions of distinct fine micro-voiding that were present, alongside of both striated and relatively featureless areas. An increasing degree of shear was seen in the dimple shapes with increasing K_{II}/K_I levels, as illustrated by Figures 11(a) and (b).

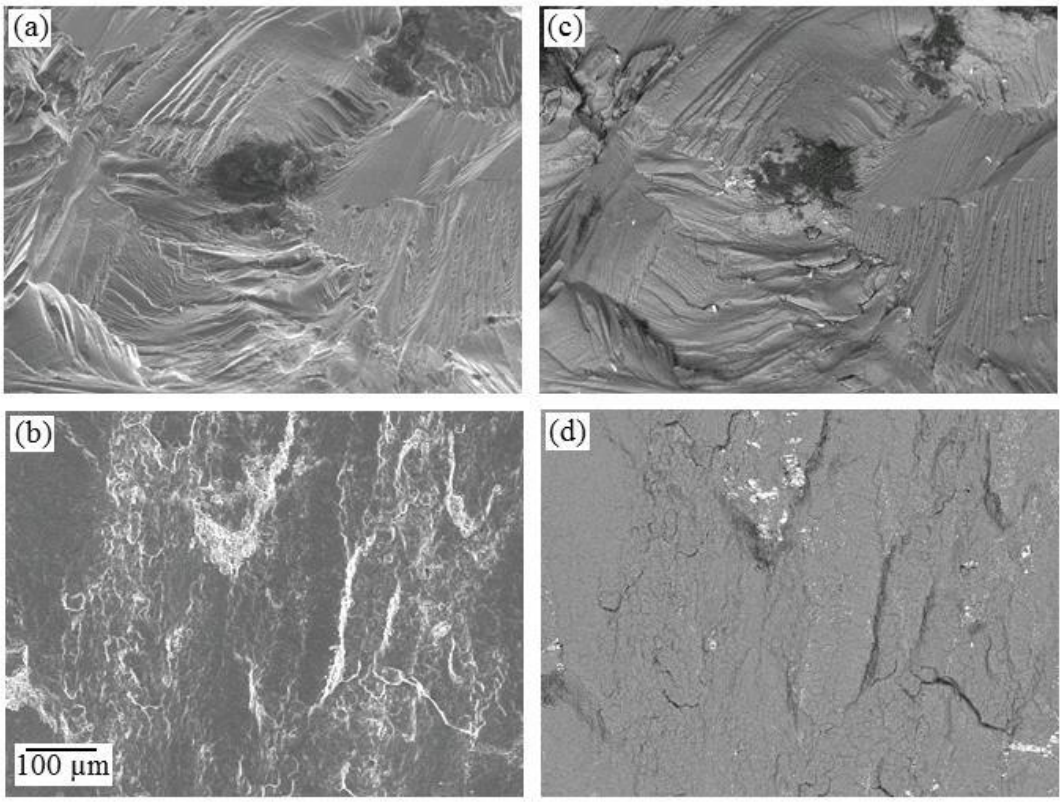

Figure 10: Fracture surfaces produced at K_{II}/K_I = 1.4, showing variations in faceting and intermetallic density with $K_{eq.max}$: (a) SEI, $K_{eq.max}$ = 5 MPa√m, (b) SEI, $K_{eq.max}$ = 15 MPa√m, (c) BEI, $K_{eq.max}$ = 5 MPa√m, (d) BEI, $K_{eq.max}$ = 15 MPa√m.

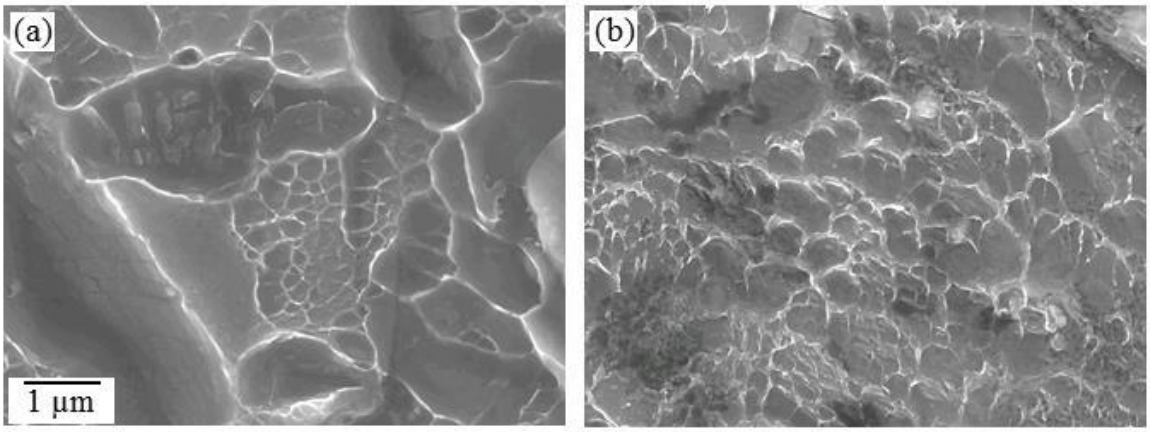

Figure 11: Dimples at $K_{eq.max}$ = 15 MPa√m, showing increasingly sheared nature at higher mixity levels: (a) SEI, K_{II}/K_I = 0, (b) SEI, K_{II}/K_I =1.4.

4. Discussion

• *Crack Path Behaviour:*

It is evident that sustained co-planar mixed mode crack propagation along grain boundaries is promoted in the present AA2297 material by increasing stress intensity levels and loading mixity. As with AA7050 tested previously, it is seen that the departure from 'conventional' mixed mode behaviour (i.e. deflection of cracks under mixed mode loading towards a predominantly tensile opening) is reasonably well characterised using the two parameters, $K_{eq.max}$ and K_{II}/K_I. For AA7050 the criteria for sustained co-planar crack propagation were identified as $K_{eq.max} \geq 15\text{MPa}\sqrt{\text{m}}$ and $K_{II}/K_I \geq 0.7$. AA2297 exhibits functionally similar behaviour and, as shown in Figure 7, the AA2297 has a similar mixity criterion ($K_{II}/K_I \geq 0.7$), whilst it appears more 'sensitive' to $K_{eq.max}$, with the criterion for sustained co-planar growth being $K_{eq.max} \geq 10\ \text{MPa}\sqrt{\text{m}}$. Thus, even though 3rd generation Al-Li alloys like the present one possess reduced ductility anisotropy compared to earlier generations of Al-Li alloys, analysis of AA2297 reveals that sensitivity to anomalous mixed mode fracture behaviour is stronger than in the AA7050 alloy.

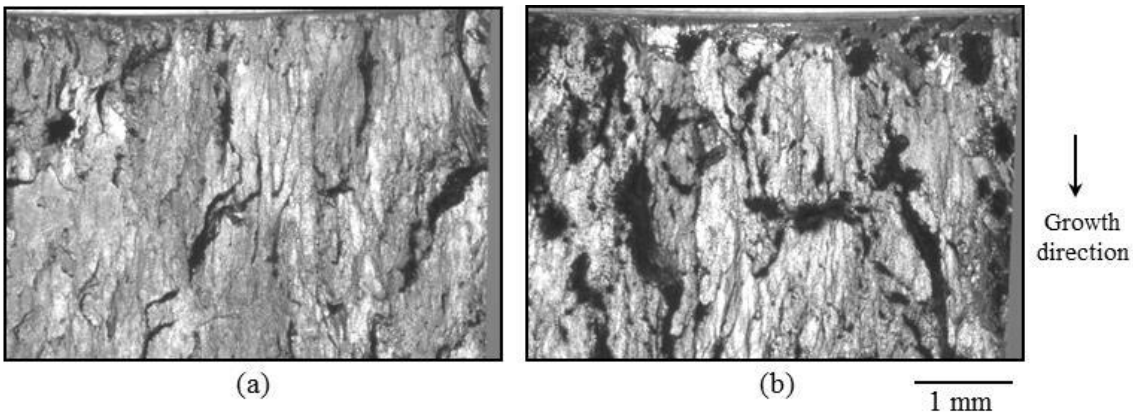

Figure 12: Effect of R-ratio on macroscopic fracture surface appearance (immediately below starter notch) under $K_{II}/K_I = 1.4$ loading, showing variation in coverage of characteristic black fretting product (hydrated oxide): (a) $R = 0.5$, and (b) $R =$ of 0.1.

The crack propagation tests show that increased K_{II}/K_I levels induce crack growth parallel to the LT plane (Fig. 7), i.e. in the direction of the long axis of the grains, and SEM fractography shows that this is associated with intergranular failure. The fact that **this** co-planar growth is favoured by increased K_{II}/K_I levels (values ≥ 0.7) is consistent with boundary failure being promoted by shear strain concentration parallel to the grain boundary PFZs [9]. It is of course significant to note that maximum stress intensity, as opposed to stress intensity range, appears to control the crack path for a given mixity ratio. It is then implied that quasi-static fracture modes (see e.g. [56]) exert a controlling influence on crack

path, consistent with the fine grain boundary voiding seen on the fracture surfaces of both the 2297 and 7050 materials. The incidence of increasing grain boundary shear strain was evident in the higher mixity fracture surfaces (transition to shear voids), although this is not a direct indication of fracture resistance.

Identifying static mode failure (void formation) at grain boundaries as the crack path controlling mechanism, it is valuable to consider the effects of changing load conditions on failure. Micromechanical changes with increasing mixity ratio may include increasing shear strain concentration along the grain boundaries, however a commensurate decrease in crack tip stress triaxiality levels will also occur. Reduction in stress triaxiality is of course expected in the transition from mode I to mode II loading in a homogeneous, isotropic medium, whilst finite element modelling confirms the same effect [57] for cracks in thin metal interlayer bonding of ceramics (somewhat analogous to the present layered/PFZ alloy structure). With failure occurring via ductile void formation at the grain boundaries, conflicting or compensatory effects on failure resistance are therefore expected with varying mixity. Whilst additional quantitative analysis of stress and deformation conditions in the matrix/PFZ layered structure of these materials would be valuable, a competition in shear strain and triaxiality effects may be consistent with the increasing propensity for co-planar crack extension on increasing mixity ratio from 0.35 to 0.7, whilst there is only a limited effect for a further increase in mixity to 1.4 (the corresponding $K_{eq.max}$ conditions for co-planar crack extension do not change).

• *Crack Growth Behaviour*

Compared in terms of ΔK_{eq}, faster crack growth rates were recorded in tests at the higher R-ratio tested (Fig. 8). For the mode I tests, the divergence of R = 0.5 and 0.1 data with increasing K levels, and the observation of static failure modes on the fracture surfaces implies the higher growth rates of the R = 0.5 tests is primarily a static failure modes effect (e.g. see [58]): this is consistent with K_{max} levels in the mode I, R = 0.5 test approaching ~80% of the S-L toughness of the material. In understanding the mixed mode crack growth rate behaviour two important issues need to be identified; (i) definition of the mixed mode crack driving force, and (ii) separation of extrinsic crack tip shielding effects, particularly the sliding contact that may occur under mode II dominated loading conditions, as indicated by the presence of wear debris on the high mixity fatigue fracture surfaces at R = 0.1. It should also be noted that identifying a crack driving force parameter and mixity dependent shielding effects is complicated by the fact that mode I and II crack tip opening loads are not attenuated in a simple equivalent manner by sliding contact: - under mode II dominated conditions, mode I crack tip opening may in fact be increased by sliding asperity contact, as pushing asperities over one another wedges open the crack tip [59]. In the first instance, it may be expected that for a given ΔK_{eq}, sliding contact effects are decreased with increasing R-ratio, consistent with the distinct reduction in fretting product seen macroscopically on the fracture

surfaces of the mixed mode tests going between R = 0.1 and 0.5, see Figure 12. As such, the K_{II}/K_I = 1.4, R = 0.5 growth rate results in Figure 8 may be expected to most closely approach closure-free mixed mode crack growth: growth is seen to be faster than under mode I in this case, with increasing shear loading then appearing to both promote and accelerate grain boundary failure. For the R = 0.1 tests, there is no discernable, simple trend in mixity effect on crack growth: presuming the R = 0.5 growth rate results are a more accurate indication of mixity influence on intrinsic crack growth behaviour, then the complex band of growth data for the R = 0.1 tests is consistent with sliding contact effects in the mixed mode, low R-ratio tests slowing mixed mode growth to some extent, the degree of which will vary with both mixity and crack length.

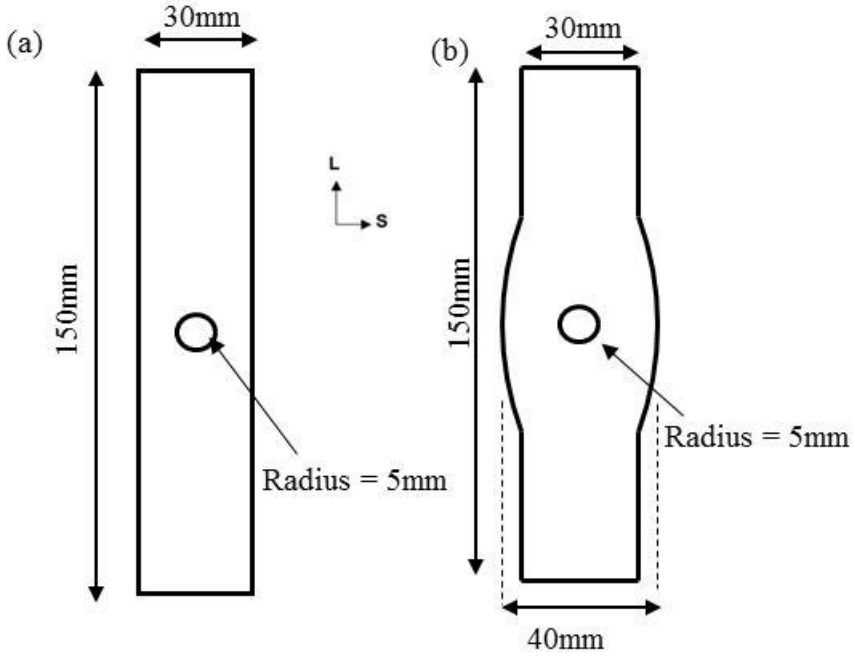

Figure 13: Schematic view of the open hole sample designs: (a) Open hole sample and (b) Modified open hole sample

• *Predicting crack paths*

The present approach can be applied to predict sustained macroscopic crack deflection. In a first attempt to verify the present concepts, samples with a centre hole were tested by a collaborator in the present work, Centre de Recherche de Voreppe (CRV, currently part of Constellium). Two geometries were considered; plain samples containing a centre hole (K_t =2.3), and a modified sample with a bulged centre-section, as shown schematically in Figure 13. The two designs will have different local stress state at the crack tip for a given crack length, particularly the higher order stress terms. Tests were performed at with nominal stress ranges from 130 to 280MPa, all at R=0.1, frequency 20 Hz in lab air.

Consistent with the approach outlined above, early crack propagation was nominal to the applied loading, and during continued propagation, a sharp transition to deflected grain

boundary failure was observed. This deflection occurred at a distance from the hole between 8.8 and 18 mm, depending on sample geometry and stress range. The stress state at the point of the crack deflection was assessed using finite element models of the samples with an added crack consisting of a variable length ligament normal to the nominal stress direction, with a deflected kink inclined at 90˚ which was set to a nominal 2mm length. For each stress range, the ligament length (i.e. the crack length at deflection) which corresponded to conditions of $K_{II}/K_I \geq 0.7$ and $K_{eq.max} \geq 10\text{MPa}\sqrt{\text{m}}$ was calculated. For all 19 experiments conducted, the measured ligament length matched the calculated ligament length well, typically within 15%, see Fig. 14. This confirms that the proposed approach for prediction of crack deflection is also suitable for centre hole samples.

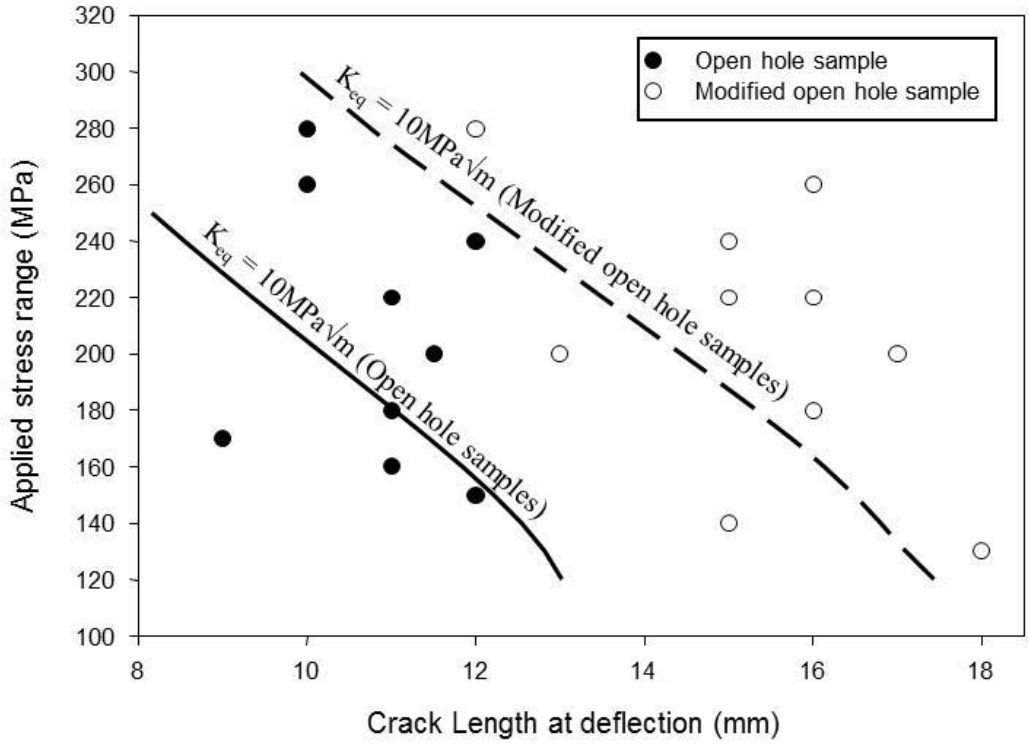

Figure 14: Crack length prior to macroscopic deflection as a function of applied stress range. Also shown are lines of constant K_{eq} = 10MPa√m for each sample design

Very recently, van der Veen et al. [60] assessed the implications of the combined K_{II}/K_I and $K_{eq.max}$ conditions identified in the present work for finite element modelling of crack paths in a range of fatigue tests on an AA2050-T84 (Al-Cu-Li) and an AA7010-T7541 (Al-Zn-Mg) alloy. In [60] fatigue tests (at R=0.1) were conducted using compact tension specimens with a range of angles between loading direction and L-T plane which produced cracks of a range of shapes: straight, curved and branched [6060]. To model the crack path they modified the model due to Pettit et al. [61] to include the present combination of K_{II}/K_I and $K_{eq.max}$ conditions and generally found good correspondence experimental and predicted

crack paths [60]. Also FCG tests on a AA2050-T8 30 mm plate by Danielou and Ehrstrom [11] conducted at a range of K_{II}/K_I and $K_{eq.max}$ conditions reveal crack growth angles that are consistent with the functionalities seen in Fig. 7.

In summary, in the present work and in [60] the combined K_{II}/K_I and $K_{eq.max}$ conditions have been applied to a range of sample geometries and orientations (Figs. 5, 13, 14) and loading conditions on a range of high strength orthotropic aluminium alloys (two 3rd generation Al-Li based alloys and two 7xxx alloys), and combined with finite element models for crack progression. In all cases a good correspondence between predicted and experimentally determined crack deflection / crack paths was evidenced. It is thus expected that the present treatment, possibly with further refinements, can be implemented in finite element based damage models, leading to improved design of improved, lighter primary aircraft structures employing novel high strength, orthotropic alloys.

5. Conclusions

- The third generation Al-Li alloy AA2297 in hot rolled plate and aged to T8 condition is found to be susceptible to sustained mixed mode failure along grain boundaries, and the behaviour is mechanistically and functionally closely consistent with established 7xxx alloy behaviour. Crack paths are seen to be controlled by a combination of crack loading mixity and maximum strain energy release rates.
- The combined K_{II}/K_I and $K_{eq.max}$ conditions for crack deflection proposed in this work appear to be able to capture crack deflection in several 3rd generation Al-Li and AA7xxx alloys.
- The propensity for grain boundary fatigue crack growth is increased by shear loading parallel to the grain boundary plane. Crack growth rates appear to be accelerated by mixed mode loading at the high R-ratio tested, but appears approximately consistent with mode I behaviour at low R-ratio, consistent with the increased surface rubbing inherent with mode II loading at low R-ratios.
- There is evidence that shear strain concentration parallel to grain boundary PFZs both promotes and accelerates grain boundary fatigue crack growth.

6. Acknowledgments

The authors would like to acknowledge the financial and material support provided by Alcan CRV. Drs J.-C. Ehrstrom (CRV, Constellium, France) and S. van der Veen (Airbus Operations SAS, France) are acknowledged for valuable discussions.

7. References

1 R.J.H. Wanhill and G.H. Bray, Fatigue Crack Growth Behavior of Aluminum–Lithium Alloys, in Aluminum-lithium Alloys, edited by N. Eswara Prasad, Amol A. Gokhale and R.J.H. Wanhill, Butterworth-Heinemann, Boston, 2014, 381-413.
2 R.J. Rioja and J. Liu, Metall Mater Trans A 43, 2012, 3325.
3 K.T. Venkateswara Rao and R.O. Ritchie, Intern Mater Rev 37, 1992, 153-185.
4 M.C. Messner, A.J. Beaudoin and R.H. Dodds, Int J Fract 188, 2014, 229–249.
5 P.S. De, R.S. Mishra, J.A. Baumann, Acta Mater 59, 2011, 5946-5960.
6 I. Sinclair, P.J. Gregson, 8090, Scr Metall Mater 30, 1994, 1287-1292.
7 K.T. Venkateswara Rao, Y. Wu and R.O. Ritchie, Met. Trans. A 19 1988, 549.
8 M.J. Crill, D. J. Chellman, E. S. Balmuth, M. Philbrook, K. P. Smith, A. Cho, M. Niedzinski, R. Muzzolini, J. Feiger, Mater Sci Forum 519-521, 2006, 1323-1328,.
9 I. Sinclair and P.J. Gregson, Mater Sci Forum 242, 1997, 175.
10 J.J. Schubbe, Eng Fract Mechanics, 76, 2009, 1037-1048.
11 A. Danielou, J.-C. Ehrstrom, US B2, 2012.
12 Yi Lin Wang, Qing Lin Pan, Li Li Wei, Bo Li, Ying Wang, Mater Design 55, 2014, 857-863.
13 B. Decreus, A. Deschamps, P. Donnadieu, J.C. Ehrström, Mater Sci Eng A 586, 2013, 418-427.
14 T.F. Morgeneyer, M.J. Starink, S.C. Wang, I. Sinclair, Acta Mater 56, 2008, 2872-2884
15 Sai-fei Zhang, Wei-dong Zeng, Wen-hua Yang, Chun-ling Shi, Hao-jun Wang, Mater & Design, 63, 2014, 368-374.
16 T. Pasang, N. Symonds, S. Moutsos, R.J.H. Wanhill, S.P. Lynch, Eng Failure Analysis, 22, 2012, 166-178.
17 Y. Chen, K.O. Pedersen, A.H. Clausen, O.S. Hopperstad, Mater Sci Eng A, 523, 2009, 253-262.
18 Zhiyi Liu, Fudong Li, Peng Xia, Song Bai, Yanxia Gu, Dier Yu, Sumin Zeng, Mater Sci Eng A, 625, 2015, 271-277
19 N. Kamp, N. Gao, M.J. Starink, I. Sinclair, Intern J Fatigue 29, 2007, 869-878.
20 A.K. Vasudévan and R.D. Doherty, Acta Metall, 35, ,1987, 1193.
21 Lili Wei, Qinglin Pan, Hongfeng Huang, Lei Feng, Yilin Wang, Intern J Fatigue 66, 2014, 55-64.
22 T. Kawabata and O. Izumi, Acta Metall, 24, 1976, 817
23 G.T. Hahn and A.R. Rosenfield, Metall Trans A 6, 1975, 653.
24 O.E. Alarcan, A.M.M. Nazar and W.A. Monteiro, Mater Sci Eng A 138, 1991, 275.
25 D.S. Thompson, Metall. Trans. A, 6A, 1975, 671.
26 J.J. Lewandowski, Y.S. Kim and N.J.H. Holroyd, Metall Trans A 23, 1992, 1679.
27 K.T. Venkateswara Rao, R.O. Ritchie, Mater Sci Techn 5, 1989, 883
28 S.P. Lynch, A.R. Wilson and R.T. Byrnes, Mater Sci Eng A 172, 1993, 79.
29 J.J. Lewandowski and N.J.H. Holroyd, Mater Sci Eng A 123, 1990, 219.
30 E.D. Sweet, S.P. Lynch, C.G. Bennett, I.J. Polmear, R.B. Nethercott and I. Musulin, in Aluminium Alloys - Their Mechanical and Physical Properties, Proc. 4th Int. Conf. on Aluminium Alloys, eds. Sanders, T.H. and Starke, E.A., Atlanta: Georgia Institute of Technology, vol. 1, 321 (1994).
31 G. Lütjering and A. Gysler, in Aluminium Alloys - Their Mechanical and Physical Properties, Proc. 1st Int. Conf. on Aluminium Alloys, eds. Sanders, T.H. and Starke, E.A., Warley: EMAS, vol. 3, 1547 (1986)
32 R.C. Dorward and D.J. Beerntsen, Metall. Mater. Trans. A, 26A, 1995, 2481
33 B. Morere, J.C. Ehrstrom, P.J. Gregson, I. Sinclair, Metall Mater Trans A 31, 2000, 2503–2515
34 M. Gräf, E. Hornbogen, Acta Metall 24, 1977, 883.
35 B. Milkereit, M.J. Starink, Mater Design, 76, 2015, 117-129.
36 M.J. Starink, B. Milkereit, Y. Zhang, P.A. Rometsch, Mater Design, 88, 2015, 958-971
37 Sai-fei Zhang, Wei-dong Zeng, Wen-hua Yang, Chun-ling Shi, Hao-jun Wang, Mater Design, 63, 2014, 368-374
38 C.G Bennett, S.P Lynch, R.B Nethercott, M Kerr, E.D Sweet, Mater Sci Eng A 247, 1998, 32-39.
39 A.W. Bowen, Mater Sci Techn 6, 1990, 1058.
40 N.S. Lee, J.H. Chen, P.W. Kao, L.W. Chang, T.Y. Tseng, J.R. Su, Scr Mater, 60, 2009, 340-343.

41 M.J. Starink, S.C. Wang, Acta Mater, 51, 2003, 5131-5150.
42 R.J. Wanhill, Aerospace Applications of Al-Li Alloys, in Aluminum-Lithium Alloys: Processing, Properties and Applications, eds N Eswara Prasad, A Gokhale, R.J.H. Wanhill, Elsevier, Oxford, UK (2014)
43 A. Cho, US patent US 8323426 B2, 2007.
44 D. Tsivoulas, P.B. Prangnell, Acta Mater 77, 2014, 1-16
45 Hao Yin, 'An Investigation on Alloying and Hot Deformation Behavior of 2297Aluminum Alloy', Master Thesis, 2014, Central South University, China
46 Chong Gao, Yang Luan, Jun-chuan Yu, Yue Ma, Trans Nonferrous Metals Soc China, 24, 2014, 2196-2202.
47 V. Araullo-Peters, B. Gault, F. de Geuser, A. Deschamps, J.M. Cairney, Acta Mater, 66, 2014, 199-208
48 S. Kobayashi, T. Yoshimura, S. Tsurekawa1, T. Watanabe, J. Cui, Mater Trans. 44, 2003, 1469-1479
49 D. Tsivoulas, PhD Thesis, University of Manchester, 2011
50 J.E. Kertz, P.I. Gouma, and R.G. Buchheit, Metall Mater Trans, 32A, 2001, 2561-2573
51 D. Tsivoulas, Metall Mater Trans 46A, 2015, 2342
52 H.A. Richard, in Biaxial and multiaxial fatigue, Proc. EGF3, Mechanical Engineering Publications, London, 217 (1989)
53 F. Erdogan, G.C. Sih, Trans. ASME J Basic Eng 85, 1963, 519-27.
54 G.C. Sih, Int J Fract 10, 1974, 305
55 S.C. Wang and M.J. Starink, Intern Mater Reviews 50, 2005, 193-215.
56 R.O. Ritchie, J.F. Knott, Acta Metall, 21, 1973, 639-648.
57 A.G. Varias, Z. Suo, C.F. Shih, J Mech Phys Solids 40, 1992, 485-509.
58 J.F. Knott, in Fatigue Crack Growth: 30 Years of Progress, Proc. Conf. on Fatigue Crack Growth, ed. Smith, R.A., Oxford, Pergamon Press, 37 (1984).
59 R.L. Carlson and C.J. Beevers, Eng Fract Mech, 22, 1985, 651.
60 S.O. van der Veen, H.P.A. Dijkers and R.C. Alderliesten, submitted for publication in AIAA Structures, Structural Dynamics and Materials Conference, San Diego, CA, USA, 2016.
61 R. Pettit, B. Annigeri, W. Owen and P. Wawrzynek, Eng Fract Mech 102, 2013, 1–14.